Biomaterials 234 (2020) 119772

Contents lists available at ScienceDirect

Biomaterials

journal homepage: www.elsevier.com/locate/biomaterials

Remodeling extracellular matrix based on functional covalent organic framework to enhance tumor photodynamic therapy

Shi-Bo Wang[a,b,1], Zhao-Xia Chen[a,1], Fan Gao[a], Cheng Zhang[a], Mei-Zhen Zou[a,b], Jing-Jie Ye[a], Xuan Zeng[a,*], Xian-Zheng Zhang[a,b,**]

[a] Key Laboratory of Biomedical Polymers of Ministry of Education & Department of Chemistry, Wuhan University, Wuhan, 430072, PR China
[b] Institute for Advanced Studies (IAS), Wuhan University, Wuhan, 430072, PR China

ARTICLE INFO

Keywords:
Photodynamic therapy
Extracellular matrix
Covalent organic framework
Tumor inhibition

ABSTRACT

Photodynamic therapy (PDT) is a promising treatment modality for tumor suppression. However, the hypoxic state of most solid tumors might largely hinder the efficacy of PDT. Here, a functional covalent organic framework (COF) is fabricated to enhance PDT efficacy by remodeling the tumor extracellular matrix (ECM). Antifibrotic drug pirfenidone (PFD) is loaded in an imine-based COF ($COF_{TTA\text{-}DHTA}$) and followed by the decoration of poly(lactic-co-glycolic-acid)-poly(ethylene glycol) (PLGA-PEG) to fabricate PFD@$COF_{TTA\text{-}DHTA}$@PLGA-PEG, or PCPP. After injected intravenously, PCPP can accumulate and release PFD in tumor sites, leading to down-regulation of ECM compenents such as hyaluronic acid (HA) and collagen I. Such depletion of tumor ECM reduces the intratumoral solid stress, a compressive force exerted by the ECM and cells, decompresses tumor blood vessels, and increases the density of effective vascular areas, resulting in significantly improved oxygen supply in tumor. Furthermore, PCPP-mediated tumor ECM depletion also enhances the tumor uptake of subsequently injected Protoporphyrinl IX (PPIX)-conjugated peptide formed nanomicelles (NM-PPIX) due to the improved enhanced permeability and retention (EPR) effect. Both the alleviated tumor hypoxia and improved tumor homing of photosensitizer (PS) molecules after PCPP treatment significantly increase the reactive oxygen species (ROS) generation in tumor and therefore realize greatly enhanced PDT effect of tumor in vivo.

1. Introduction

Photodynamic therapy (PDT) is well known as a noninvasive therapeutic procedure with high selectivity for tumor inhibition. Photosensitizer (PS), light, and oxygen are three essential components of PDT [1,2]. Upon the illustration of harmless light with a specific wavelength, nontoxic PS can transfer the energy from light to oxygen to generate cytotoxic reactive oxygen species (ROS), which leads to rapid cell death through apoptosis and/or necrosis [3–5]. Given that traditional PSs are highly hydrophobic and lack of tumor selectivity, to improve the tumor homing of PSs, nanotechnologies that constructing PS-involved nanoparticles (PNPs) have been widely developed and proved to be feasible ways to improve the pharmacokinetics and tumor accumulation of PSs, which mainly rely on the enhanced permeability and retention (EPR) effect [6–8]. However, due to the poorly formed tumor vessels and irregular proliferation of tumor cells, PDT always suffers from insufficient oxygen supply and weakened EPR effect of PNPs in tumor regions, which greatly restrict the ROS generation in whole tumor and thereby significantly decrease the therapeutic outcomes of PDT in vivo [9–11].

Recent studies showed that tumors are not composed merely of tumor cells alone. Instead, they are complex systems that comprising tumor cells, non-tumor cells, and blood vessels etc., all embedded in a fibrous material network known as the extracellular matrix (ECM) [12,13]. The ECM is a critical component of the tumor microenvironment and proved to play key roles in tumor initiation, growth, metastasis, and therapy resistance [14–17]. Particularly, the ECM and cells can squeeze the tumor blood vessels, which reduces or prevents blood flow to the tumor regions, thus leading to the reduction of oxygen supply and drug delivery to tumor tissues [18–20]. Simultaneously, the abnormally rigid matrix in tumors can also act as a physical barrier to hinder the diffusion of oxygen and drugs, further limiting the

* Corresponding author.
** Corresponding author. Key Laboratory of Biomedical Polymers of Ministry of Education & Department of Chemistry, Wuhan University, Wuhan, 430072, PR China.
E-mail addresses: zeng_xuan@163.com (X. Zeng), xz-zhang@whu.edu.cn (X.-Z. Zhang).
[1] These authors contribute equally.

https://doi.org/10.1016/j.biomaterials.2020.119772
Received 10 October 2019; Received in revised form 22 December 2019; Accepted 8 January 2020
Available online 09 January 2020
0142-9612/

therapeutic efficacy of PDT [21,22]. In view of the serious obstruction of tumor ECM for PDT, utilizing matrix-depleting agents to digest tumor ECM might be a feasible way to enhance the treatment efficacy of PDT in vivo. However, since ECM components such as collagen and hyaluronic acid (HA) provide basic structure and support to bones and normal tissues [23], developing safe patterns that ensure the selectively working of matrix depleting agents in tumors is necessary and meaningful.

Covalent organic frameworks (COFs) are an emerging class of crystalline porous polymers which have gained considerable research attention in recent years [24,25]. Owing to their tunable molecular structures, high surface area, and diverse functionality, COFs are widely studied and applied in multiple fields including gas adsorption and separation, catalytic science, energy storage, and optoelectronics [26–30]. Moreover, due to the robust covalent bond linkage and the metal ion free feature, COFs also possess outstanding chemical stability as well as good biocompatibility [31,32], which show great potential for biomedical applications. Recent studies have indicated that COFs can serve as promising drug carriers with high loading capacity, appropriate release behavior, and low cytotoxicity [33–35]. Therefore, utilizing COFs for tumor targeted delivery of matrix-depleting agents in vivo is of great attraction.

Keeping all these in mind, here, a functional COF-based ECM-depleting nanosystem was developed to enhance tumor PDT. As illustrated in Scheme 1, anti-fibrotic drug pirfenidone (PFD) was loaded in an imine-linked COF termed as $COF_{TTA\text{-}DHTA}$ (TTA: 4,4′,4″-(1,3,5-triazine-2,4,6-triyl)trianiline and DHTA: 2,5-dihydroxyterethaldehyde) and followed by the decoration of amphiphilic polymer poly(lactic-co-glycolic-acid)-poly(ethylene glycol) (PLGA-PEG) to provide PFD@$COF_{TTA\text{-}DHTA}$@PLGA-PEG, or PCPP. PFD was reported can reduce the contents of ECM components such as collagen and HA [36]. $COF_{TTA\text{-}DHTA}$ was chosen because of its good chemical stability and relatively large pore size [37]. Moreover, PLGA-PEG was engaged to improve the dispersibility and biocompatibility of the nanosystem [38]. After injected intravenously, PCPP was supposed to accumulate in tumor sites via the EPR effect and release PFD in situ to down-regulate the levels of tumor ECM components, leading to the reduction of tumor solid stress. This was supposed to decompress tumor blood vessels, restore vascular functionality, and thereby improve the oxygen supply in tumor. Moreover, PCPP treatment was also expected to enhance the tumor homing of subsequently injected PPIX-conjugated peptide formed nanomicelles (NM-PPIX) which served as model PNPs due to the improved EPR effect. The improved tumor oxygenation and increased tumor uptake of PSs after PCPP treatment were supposed to promote the ROS generation in tumor upon laser irradiation, thus realizing remarkably enhanced tumor PDT effect in vivo.

2. Materials and methods

2.1. Materials

PFD and PPIX were provided by Aladdin Reagent (Shanghai, China). PLGA-PEG ($PLGA_{2000}$-PEG_{2000}) was obtained from Ponsure Biotechnology (Shanghai, China). DHTA and TTA were provided by Extension Technology Co.,Ltd (Jilin, China). Fmoc-PEG_8-CH_2CH_2COOH was provided by Biomatrik Inc. (Zhejiang, China). ROS-ID hypoxia/oxidative stress detection kit was provided by Enzo Life Sciences. Inc. (USA). Fetal bovine serum (FBS), RMPI 1640, penicillin-streptomycin, agarose, trypsin, Dulbecco's phosphate buffered saline (PBS), and MTT were obtained from Lonza Group Ltd. (Switzerland). L-012 was obtained from Wako (Japan). All other reagents were used without further purification.

2.2. Instruments

The morphologies of PCPP and NM-PPIX were examined with TEM (JEOL-2100, Tokyo, Japan) and SEM (Zeiss Sigma FESEM). XRD spectra was obtained on a Rigaku MiniFlex. The UV–vis absorbance was measured by a UV–vis spectroscopy (Lambda Bio40). Zeta potential and particle size were measured by a zeta sizer (Nano ZS, Malvern Instruments). Fluorescence images were obtained on a C1-Si (Nikon) laser scanning confocal microscope (CLSM). The histologic sections were observed with an inverted fluorescence microscope (IX 70, Olympus, Japan). In vivo imaging experiments were conducted by using IVIS imaging systems (PerkinElmer).

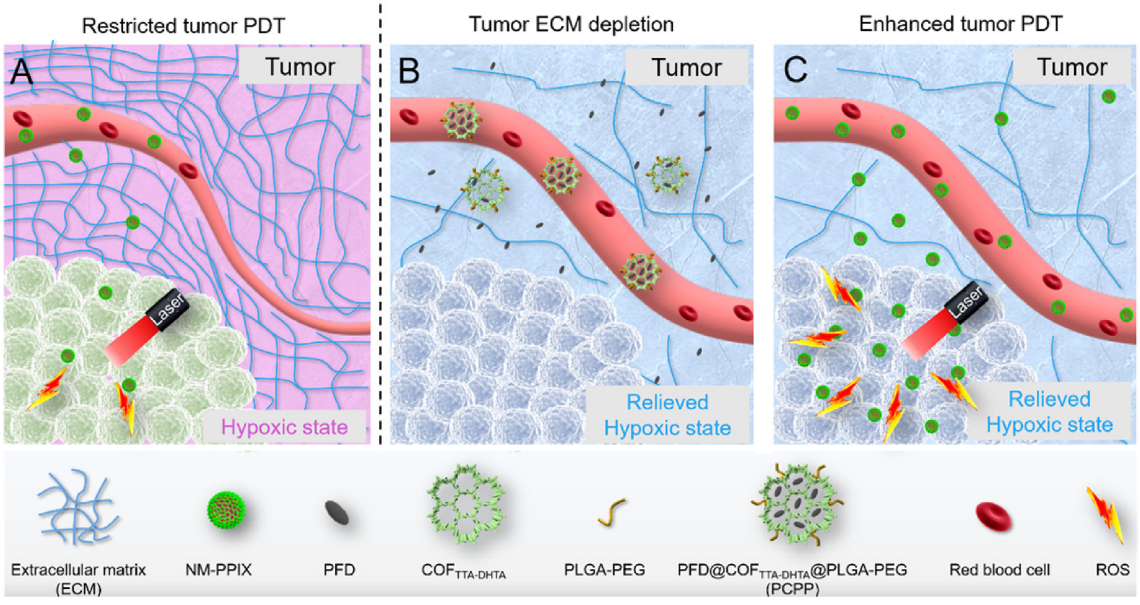

Scheme 1. Schematic illustration of PCPP-mediated tumor ECM degradation to enhance tumor PDT effect. A) Restricted tumor PDT effect due to the insufficient oxygen supply as well as the limited uptake of NM-PPIX in tumor. B) Selective delivery and release of PFD in tumor tissues by PCPP, PFD-mediated tumor ECM depletion, promotion of tumor vasculature functionality, and alleviation of the hypoxic state of tumor. C) Enhanced ROS generation and tumor PDT effect due to the improved oxygen supply and tumor uptake of NM-PPIX.

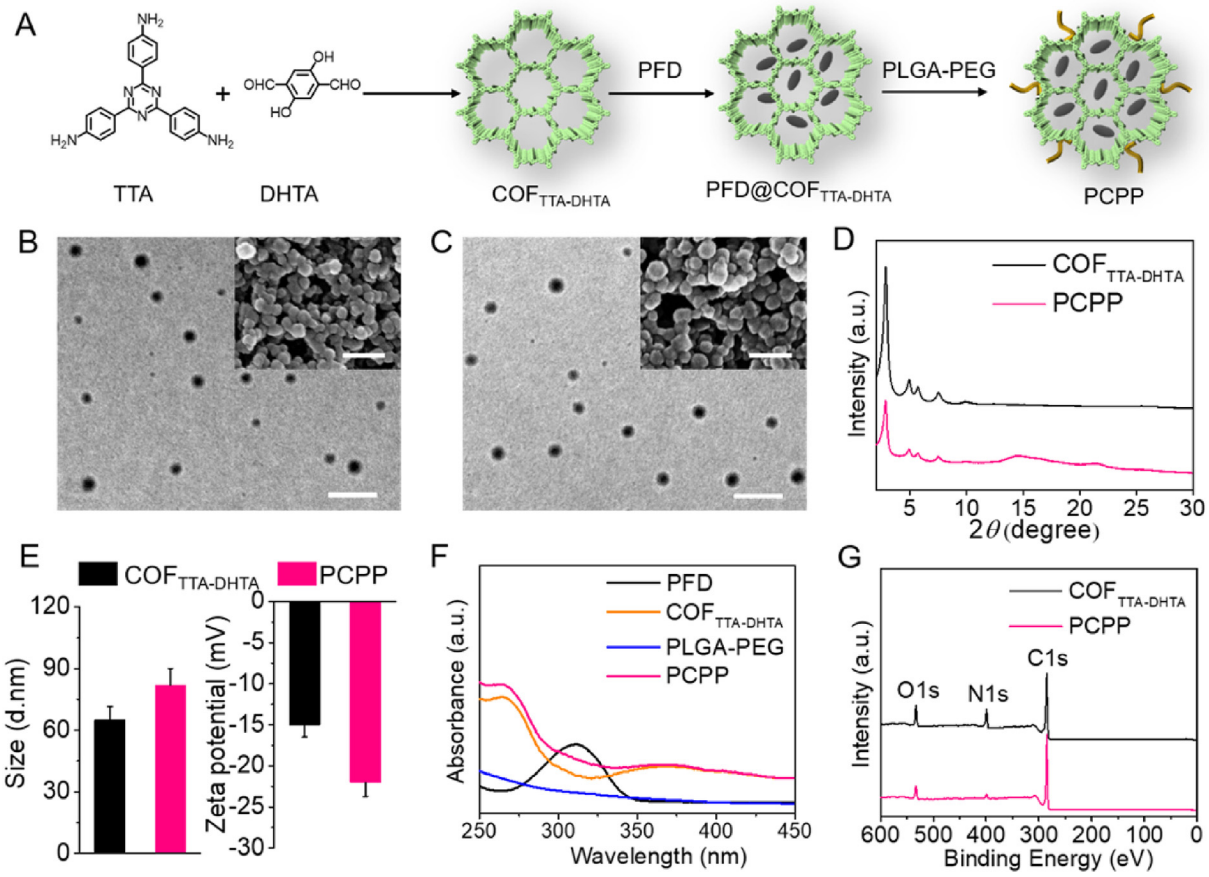

Fig. 1. A) Scheme of the preparation of PCPP. B) TEM and SEM (inset) images of $COF_{TTA\text{-}DHTA}$. Scale bar: 200 nm. C) TEM and SEM (inset) images of PCPP. Scale bar: 200 nm. D) PXRD patterns of $COF_{TTA\text{-}DHTA}$ and PCPP. E) Hydrodynamic size and ζ potential of $COF_{TTA\text{-}DHTA}$ and PCPP. F) UV–vis absorbance of PFD, $COF_{TTA\text{-}DHTA}$, PLGA-PEG, and PCPP. G) XPS spectra of $COF_{TTA\text{-}DHTA}$ and PCPP.

2.3. Preparation of $COF_{TTA\text{-}DHTA}$

Pyrex tube with the size of 10 × 8 mm (o.d × i.d) was filled with TTA (15 mg, 0.0424 mmol), DHTA (11 mg, 0.0662 mmol), dioxane (0.15 mL), mesitylene (0.85 mL), and aqueous acetic acid (100 μL, 6 M) sequentially. The mixture was dissolved through ultrasonic. The solution was degassed through three freeze-pump-thaw cycles. After naturally warmed up to room temperature, the tube was placed in oven and heated at 120 °C for 72 h. The solid was then isolated by filtration washed with THF and sequentially fluxed with THF and acetone in a Soxhlet extractor for 24 h (each solvent). After drying under dynamic vacuum at room temperature for 1 h, the temperature of COF sample was raised to 120 °C and kept for 8 h. Then the sample was cooled down to 50 °C and kept for 4 h to completely activate $COF_{TTA\text{-}DHTA}$.

2.4. Preparation of PCPP

$COF_{TTA\text{-}DHTA}$ (50 mg) was dissolved in DMSO (30 mL) in a 50 mL centrifuge tube. After dispersing with ultrasonic grinder for 30 min, PFD (100 mg) in 5 mL of DMSO was added in the centrifuge tube and the mixture was stirred at room temperature for 12 h. The superfluous PFD was removed by centrifugation at 9000 rpm for 10 min and washed with DMSO for 3 times. Then, PLGA-PEG (100 mg) in distilled water (10 mL) was poured into the prepared $COF_{TTA\text{-}DHTA}$@PFD aqueous solution and stirred at room temperature for 24 h. Excess PLGA-PEG was removed by centrifugation for 10 min and washed with distilled water for several times. Finally, PCPP was obtained via freeze-dry.

For the preparation of Cy5.5-modified PCPP, $COF_{TTA\text{-}DTA}$ was first mixed with NH_2-PEG-Cy5.5 (Mw: 2000) (w/w = 1/40) in DMSO for 6 h. The excess NH_2-PEG-Cy5.5 was removed by washing with DMSO repeatedly to obtain Cy5.5-modified $COF_{TTA\text{-}DHTA}$. Then, Cy5.5-modified PCPP was prepared the same way as PCPP that described above.

2.5. Drug release of PCPP

The drug release experiment of PCPP was investigated at 37 °C in PBS (pH 7.4). Briefly, newly synthesized PCPP stock solution (1 mL, 1 mg mL^{-1}) was added to a dialysis membrane filter (MWCO: 5000 Da), immersed into 5 mL of PBS (pH 7.4) and then shaken in a water bath at 37 °C. The PFD concentration in the release medium was determined by measuring the absorbance of the solution at 312 nm.

2.6. Preparation of PPIX-PEG-KGDD

Peptide PPIX-PEG-KGDD was prepared via a SPPS method on 2-chlorotrityl chloride resin. Fmoc-protected amino acids, Fmoc-PEG_8-CH_2CH_2COOH, and PPIX were connected to the resin in proper order. Then the peptide was cleaved from the resin using a mixture of TFA/TIS/H_2O = 95/2.5/2.5 (V/V/V). The molecular weight of the obtained product was confirmed by ESI-MS, which was calculated to be 1387, found 1386 ([M - H]$^-$).

2.7. Cell culture

Colon adenocarcinoma (CT26) cells were incubated in RMPI 1640 medium at 37 °C in a humidified atmosphere containing 5% CO_2.

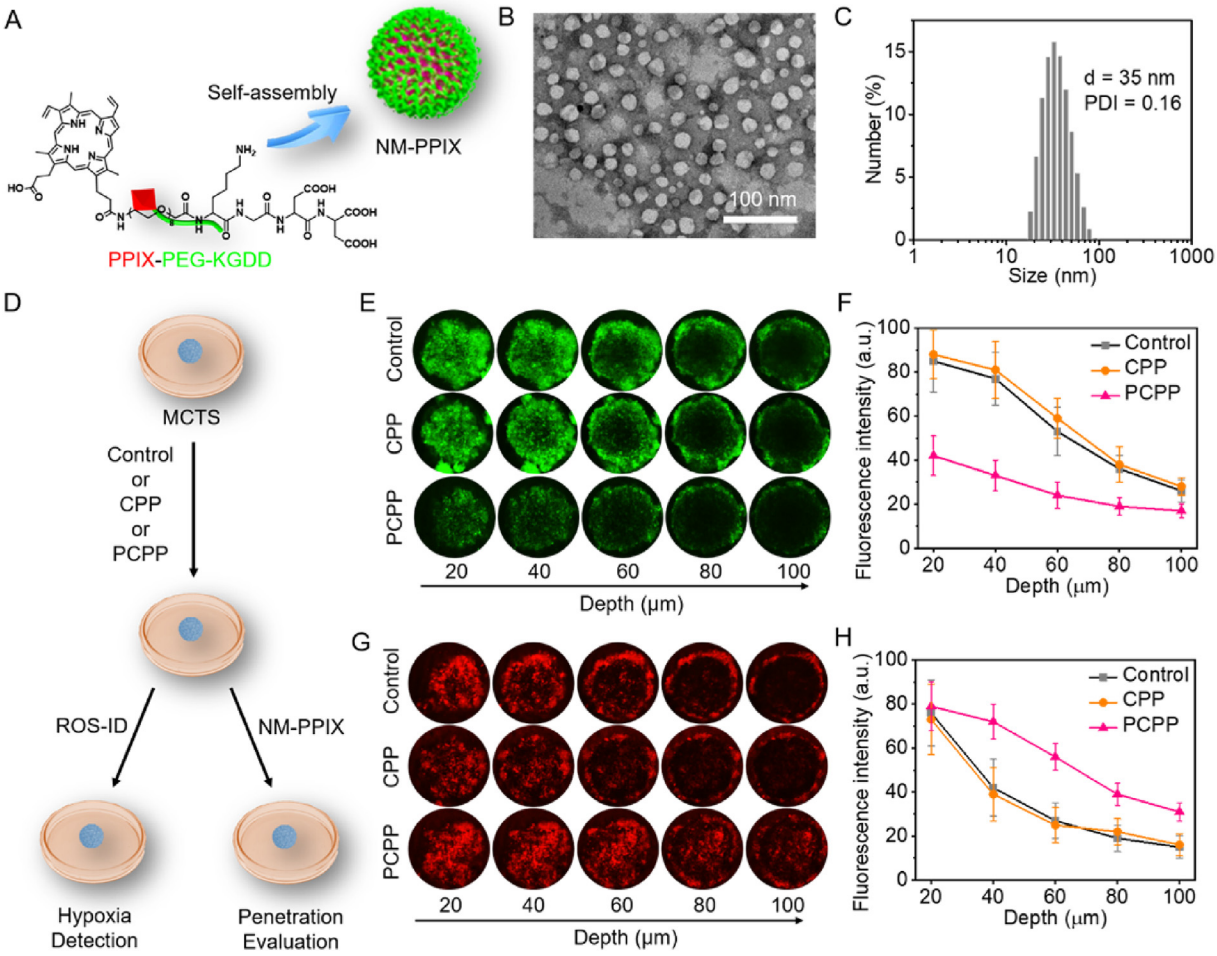

Fig. 2. A) Scheme of the self-assembly of peptide PPIX-PEG-KGDD to provide NM-PPIX. B) TEM image and C) size distribution of NM-PPIX. D) Scheme of the hypoxia detection and penetration evaluation assays in MCTS model. E) Fluorescence imaging of hypoxia in MCTS with various treatment. Hypoxic cells showed green fluorescence. F) Fluorescence intensity of MCTS in E) at different depths. G) Fluorescence imaging of NM-PPIX penetration depth in MCTS with various treatments. NM-PPIX showed red fluorescence due to the fluorescence of PPIX. H) Fluorescence intensity of MCTS in G) at different depths. (For interpretation of the references to colour in this figure legend, the reader is referred to the Web version of this article.)

2.8. MCTS culture

CT26 MCTS were prepared as reported previously. In brief, CT26 cells were seeded into a 96-well plate which pre-layed 1% (w/v) agarose gel and continuously incubated at 37 °C for 7 days.

2.9. Hypoxia detection and PNPs penetration in MCTS

When the sizes reached about 300 μm, CT26 MCTS were first treated with PCPP (PFD concentration: 100 μg mL^{-1}), CPP, or without treatment (control) for 72 h and then the cell culture media were removed. For hypoxia detection, MCTS were added with 100 μL of ROS-ID (8×10^{-7} M) and incubated for 30 min. Subsequently, the MCTS were observed via CLSM. For PNPs penetration detection, NM-PPIX (20 μg mL^{-1}) was added to the MCTS and incubated for 4 h. Then the MCTS were washed with PBS and observed by CLSM.

2.10. Animals and tumor model

BALB/c mice (female, 4–5 weeks old) were purchased from Wuhan University Animal Biosafty Level III Lab. All animal experiments were approved by the institutional animal use and care regulations of Wuhan University (Wuhan, China). All animal experimental procedures were in accordance with the Institutional Animal Care and Use Committee (IACUC) of the Animal Experiment Center of Wuhan University (Wuhan, China). Tumor model was created by subcutaneous injecting CT26 cells (1×10^7) in the right back of each mouse.

2.11. Evaluation of biodistribution of PCPP

Cy5.5-modified PCPP was constructed to investigate the biodistribution of PCPP. Compared with PCPP construction, Cy5.5-PEG-NH_2 was first convalently attached to the surface of $COF_{TTA\text{-}DHTA}$ via Schiff base reaction and then followed by PFD loading and PLGA-PEG modification. CT26-tumor-bearing mice (tumor size about 100 mm^3) was intravenously injected with the Cy5.5-modified PCPP and sacrificed at 24 h post injection. The tumor tissue and major organs were collected and imaged using a small animal imaging system.

2.12. Elastic modulus measurement

When the size of tumors reached about 100 mm^3, PBS, CPP or PCPP (100 μL, 50 mg kg^{-1}) was injected into the tumor-bearing mice for a continuous 7 days. On the 10th day, mice were sacrificed and the tumors from various groups were collected to evaluate the elastic modulus under compression model. The max strain was set as 80% to protect the tester.

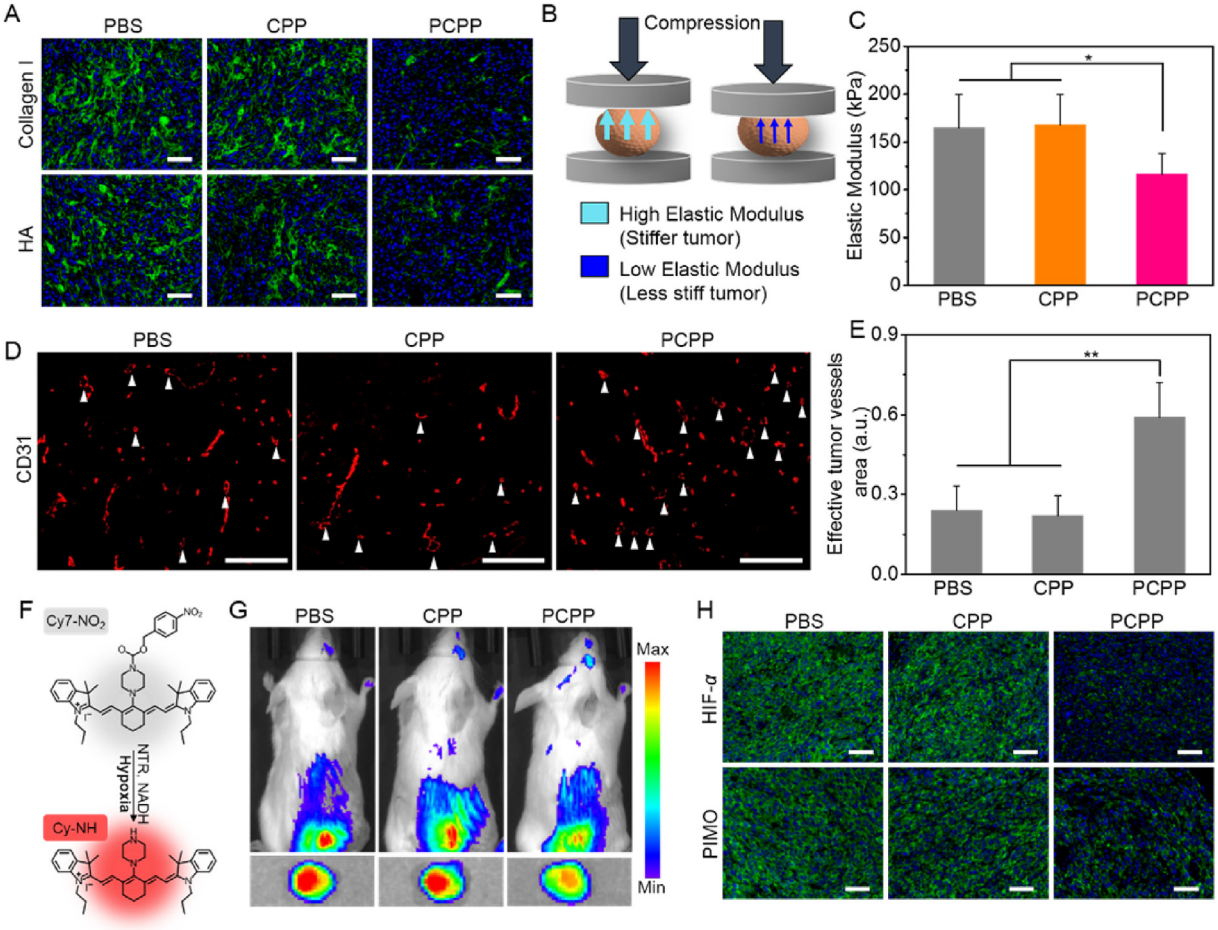

Fig. 3. A) Expression of Collagen I and HA in tumors detected by immunocytochemistry of mice after various treatments. Scale bar: 50 μm. B) Scheme of the relationship between elastic modulus and tumor stiff. C) Elastic modulus of tumors from mice after different treatments (n = 3, *p < 0.05). D) Representative fluorescence images of tumor blood vessels of tumor slices stained by anti-CD31. E) area of effective tumor vessels with different treatments (n = 3, **p < 0.01). Scale bar: 100 μm. F) Scheme of Cy7-NO_2 mediated hypoxia detection in vivo. G) In vivo fluorescence imaging of mice ex vivo fluorescence imaging of tumor tissues for hypoxia detection using Cy7-NO_2. H) Representative fluorescence images of tumor slices from mice with various treatments stained with HIF-1α tracer and pimonidazole. Scale bar: 50 μm.

2.13. In vivo hypoxia detection

When the size of tumors reached about 100 mm^3, PBS, CPP or PCPP (100 μL, 50 mg kg^{-1}) was injected into the tumor-bearing mice for a continuous 7 days. On the 10th day, mice were intravenously injected with Cy7-NO_2 (100 μL, 10 μM) and imaged via the IVIS imaging systems. At 24 h post Cy7-NO_2 injection, mice were sacrificed and the tumors were harvested and imaged via the small animal imaging system.

2.14. In vivo biodistribution of NM-PPIX

When the tumor sizes reached about 100 mm^3, mice were intravenously injected with PBS, CPP or PCPP (100 μL, 50 mg kg^{-1}) for a continuous 7 days. On the 10th day, mice were intravenously injected with NM-PPIX (100 μL, 20 mg kg^{-1}) and the in vivo biodistribution of NM-PPIX was detected via the IVIS imaging systems. Besides, mice were sacrificed at 24 h post NM-PPIX injection and the major organs and tumor tissues were collected and imaged via the small animal imaging system (Ex: 640 nm, Em: 680 nm).

2.15. In vivo anti-tumor studies

For therapeutic assays in vivo, 25 of CT26 tumor-bearing mice were divided into five groups and treated according to the timeline in Fig. 5A (Group 1: PBS; Group 2: PCPP (100 μL, 50 mg kg^{-1}) + NM-PPIX (100 μL, 20 mg kg^{-1}); Group 3: NM-PPIX + laser (0.5 W cm^{-2}, 10 min); Group 4: CPP + NM-PPIX + laser; Group 5: PCPP + NM-PPIX + laser). The tumor volume was calculated as following formula: $V = W^2L/2$ (W and L represented the shortest and longest diameters of tumors, respectively). At 24 h post laser irradiaiton, tumor tissues of mice were collected for H&E staining, TUNEL staining, and Western blot analysis. On the 19th day, the blood samples of mice were collected for blood biochemistry analysis and tumor tissues and major organs of sacrificed mice were collected for histological analysis.

2.16. In vivo ROS detection

ROS luminescent probe L-012 (100 μL, 10 μM) was injected intratumously to mice before laser irradiation. Then the mice after laser irradiation were imaged via the small animal imaging system.

2.17. Metastasis evaluation

Mice from different groups were sacrificed on the 35th day and the lung sections of mice were colleted for H&E staining.

2.18. Statistical analysis

Statistical analysis was performed using a Student's t-test. The

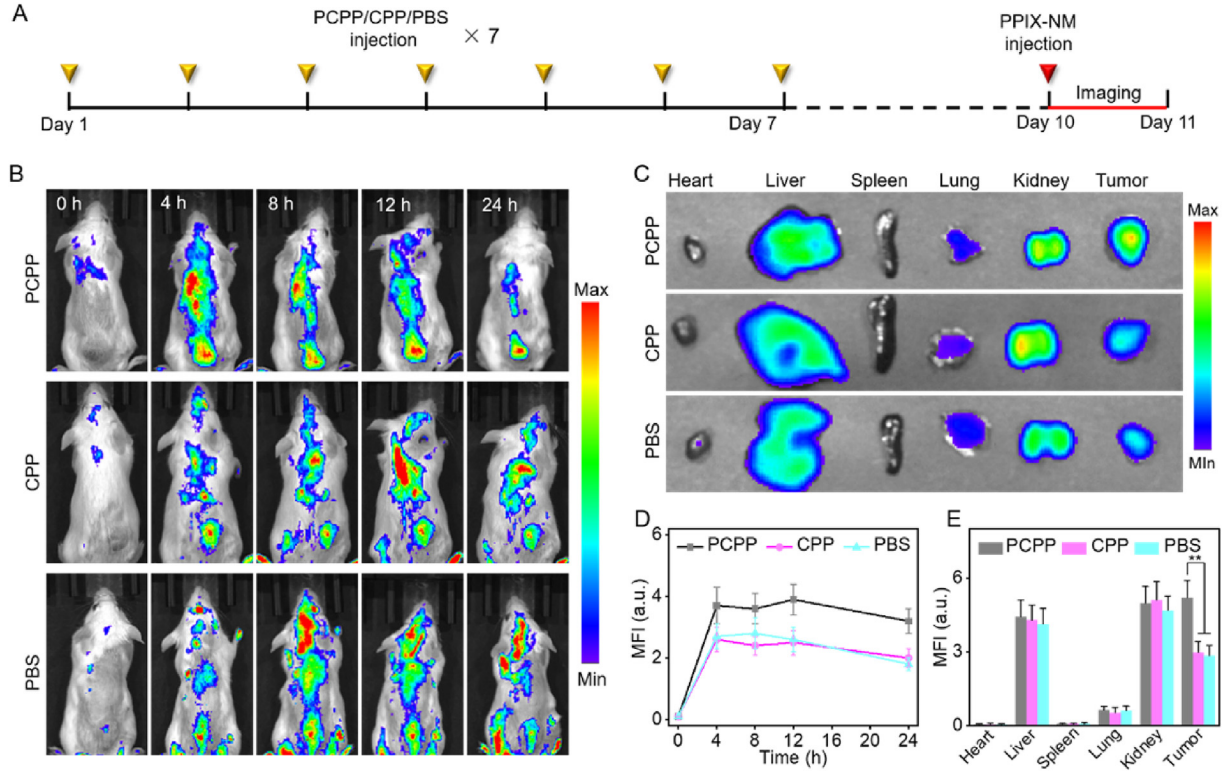

Fig. 4. A) Scheme of the timeline for in vivo fluorescence imaging of NM-PPIX. B) Real time fluorescence images of mice after the injection of NM-PPIX with various treatments. C) Ex vivo fluorescence images of major organs and tumors from groups of mice with various treatment. D) The corresponding mean fluorescence intensity in tumor sites of B). E) The corresponding mean fluorescence intensity of C) (n = 3, **p < 0.01).

values were presented as mean ± standard deviation (SD). The differences were considered to be statistical significant for p value < 0.05 (*p < 0.05, **p < 0.01, ***p < 0.001).

3. Results and discussion

3.1. Preparation and characterization of PCPP

$COF_{TTA\text{-}DHTA}$ nanoparticles were prepared through solvothermal reaction of hexa-topic DHTA building block with TTA (Fig. 1A), where the imine bonds ensured the formation of $COF_{TTA\text{-}DHTA}$ with good crystallinity (Fig. S1). Transmission electron microscoy (TEM) and Scanning electron microscopy (SEM) images in Fig. 1B clearly featured the uniform nanostructure of $COF_{TTA\text{-}DHTA}$ with a size of about 60 nm. Characteristic peak at 1623 cm^{-1} in Fourier transform infrared (FTIR) spectrum suggested the formation of characteristic imine bonds (Fig. S2) [32]. Besides, the powder X-ray diffraction (PXRD) patterns of the as-prepared $COF_{TTA\text{-}DHTA}$ (Fig. 1D) matched well with those previously reported [37], indicating the highly crystalline of the product. In addition, X-ray photoelectron spectroscopy (XPS) result in Fig. 1G demonstrated that $COF_{TTA\text{-}DHTA}$ mainly possessed elements of C (285.69 eV), N (398.05 eV) and O (530.88 eV). Moreover, $COF_{TTA\text{-}DHTA}$ possessed large Brunauer-Emmett-Teller (BET) surface area of 2831 $m^2\ g^{-1}$ and pore size of 3.67 nm as evidenced by N_2 absorption analysis (Fig. S3), indicating the good potential of $COF_{TTA\text{-}DHTA}$ for drug loading. For PCPP fabrication, PFD was encapsulated into $COF_{TTA\text{-}DHTA}$ by ultrasonic mixing and then amphiphilic PLGA-PEG was decorated on the surface of hydrophobic $COF_{TTA\text{-}DHTA}$ via hydrophobic interaction. TEM and SEM images in Fig. 1C indicated spherical morphology of PCPP with a narrow size distribution. Fig. 1E shows that the hydrodynamic size of PCPP was detected to be 82 ± 8 nm (PDI: 0.12) by dynamic light scattering (DLS), which was a little larger than $COF_{TTA\text{-}DHTA}$ (65 nm, PDI: 0.14). Besides, PXRD analysis revealed the retained crystal structure of $COF_{TTA\text{-}DHTA}$ in PCPP (Fig. 1D). The successful loading of PFD in PCPP was also confirmed by ultraviolet–visible (UV–vis) spectra in Fig. 1F and the loading efficiency was calculated to be 32 ± 4 wt%. The relatively high drug loading efficiency was mainly attributed to the large BET surface area and pore size of $COF_{TTA\text{-}DHTA}$. Furthermore, during PCPP fabrication, the ζ potential decreased from −15 eV ($COF_{TTA\text{-}DHTA}$) to −22 eV (PCPP) (Fig. 1E). Additionally, XPS result (Fig. 1G) as well as the FTIR spectra (Fig. S2) further proved the efficient drug loading and polymer modification. Of special note, owing to the introduction of hydrophilic PEG sequence, PCPP exhibited good dispersion in water, phosphate buffer saline (PBS), and culture medium (containing 10% fetal bovine serum), which was different from $COF_{TTA\text{-}DHTA}$ alone that precipitated rapidly in them (Fig. S4). Moreover, drug release study showed that PFD can leached slowly from PCPP and the release rate was about 74% after incubation in PBS (pH 7.4) for 72 h (Fig. S5), which indicated the efficient drug release behavior of PCPP.

3.2. Evaluation of tumor hypoxia and nanoparticle penetration on in vitro 3D tumor model

First, whether the treatment of PCPP could relieve tumor hypoxia and enhance the penetration of PNPs by depleting ECM were evaluated on mouse colon cancer (CT26) multicellular tumor spheroids (MCTS) which served as in vitro 3D tumor models. Compared with monolayer adherent cells, MCTS possess several characteristics of in vivo tumors including hypoxic core and dense ECM, which are versatile 3D models for tumor biology study and drug penetration assessment [39]. In this study, a commonly used fluorogenic probe ROS-ID, whose fluorescence is proportional to the hypoxia degree was chosen for the oxygenation state evaluation [40]. Meanwhile, NM-PPIX which formed by the self-assembly of a PS-conjugated peptide PPIX-PEG-Lys-Gly-Asp-Asp (PPIX-PEG-KGDD) were prepared as model PNPs for penetration evaluation (Fig. 2A). TEM image in Fig. 2B indicated the spherical morphology of

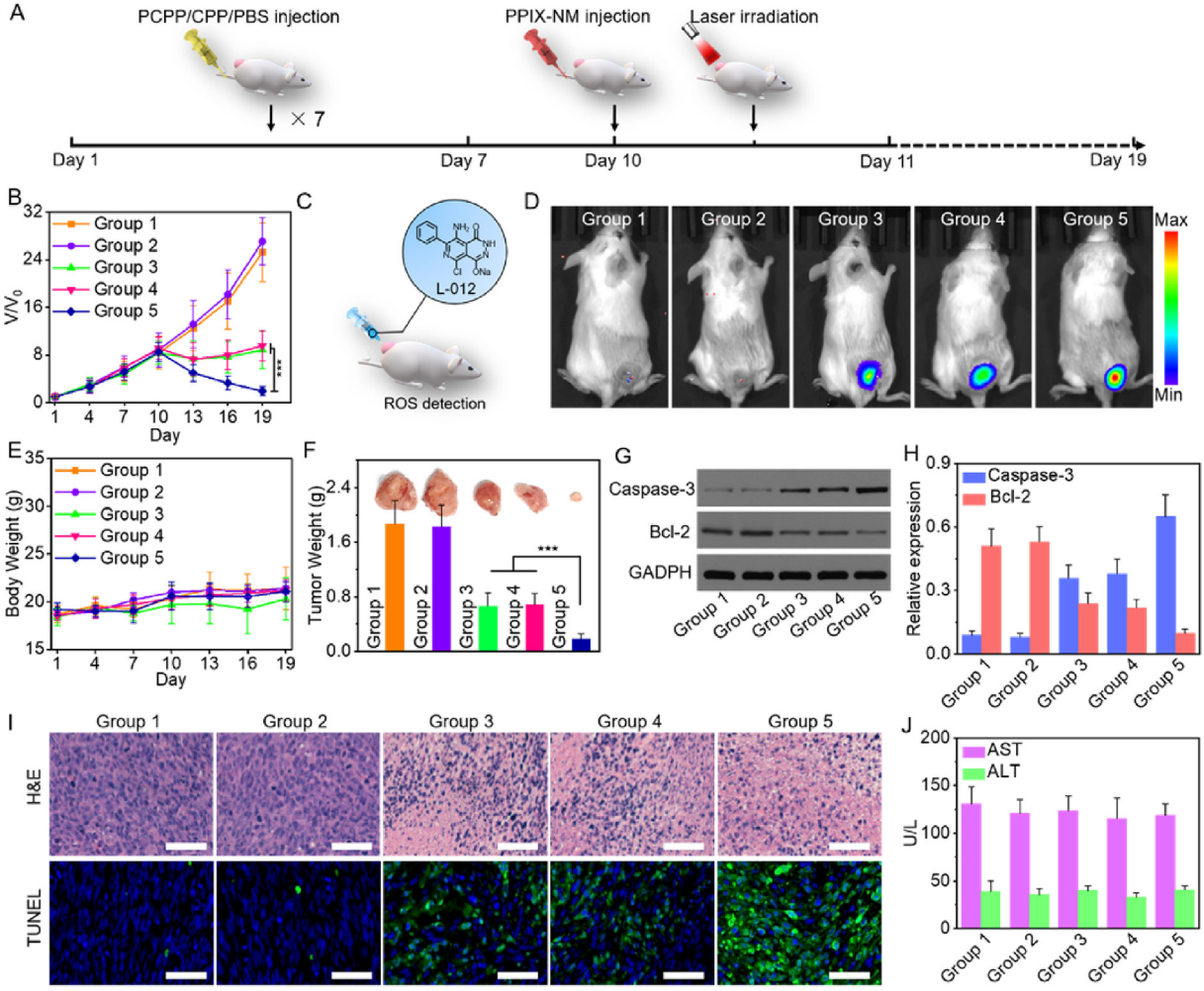

Fig. 5. A) Scheme of the timeline for the anti-tumor treatment. B) Tumor volume curve of different groups of mice after various treatments (n = 5, ***p < 0.001). C) Scheme of L-012 mediated in vivo ROS detection. D) Fluorescence imaging of mice after the injection of L-012 for in vivo ROS detection. E) Body weight changes of mice during the treatments (n = 5). F) Average tumor weights and representative pictures of tumors of different groups of mice that sacrificed on the 19th day (n = 5, ***p < 0.001). G) Caspase-3 and bcl-2 expression in tumors after various treatments. H) Corresponding quantitative results of G) (n = 3). I) Representative H &E and TUNEL staining pictures of tumors from different groups of mice. J) Blood biochemical analysis of AST and ALT in serum of mice on the 19th day (n = 3). (Group 1: PBS; Group 2: PCPP + NM-PPIX; Group 3: NM-PPIX + laser; Group 4: CPP + NM-PPIX + laser; Group 5: PCPP + NM-PPIX + laser.)

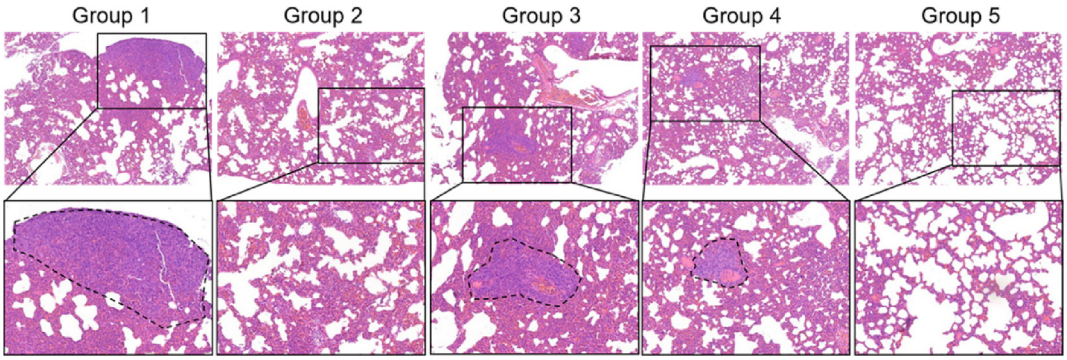

Fig. 6. Representative H&E staining pictures of lung sections from different groups of mice sacrificed on the 35th day (× 40).

NM-PPIX with uniform sizes and the average hydrodynamic diameter of NM-PPIX was detected to be about 35 nm (Fig. 2C). As illustrated in Fig. 2D, MCTS were first treated with PCPP, $COF_{TTA\text{-}DHTA}$@PLGA-PEG (CPP) or only culture medium (control group) for 3 days, respectively. Then the MCTS were incubated with ROS-ID or NM-PPIX and followed by observation under confocal laser scanning microscope (CLSM). As shown in Fig. 2E and F, compared with control group, much weaker fluorecence of hypoxia probe was observed in PCPP group. This result indicated that the hypoxia state of MCTS can be obviously relieved by PCPP treatment, which was mainly attributed to the enhanced oxygen diffusion in MCTS. Notably, the treatment of CPP showed negligible effect on the hypoxia condition of MCTS, suggesting the hyoxia improvement was owing to the presence of PFD. Moreover, as shown in Fig. 2G, PCPP treatment also greatly enhanced the penetration of NM-

PPIX in MCTS in which the fluorescence of NM-PPIX was detected at much greater depth than that in CPP or control group. And the quantitative results of Fig. 2G shows that the average fluorescence intensity of NM-PPIX in PCPP group was over 2-fold higher than that in control and CPP groups at a depth of 100 μm (Fig. 2H). These data clearly showed that PCPP can effectively alleviate the hypoxia state and enhance nanoparticle penetration in the in vitro 3D tumor models.

3.3. In vivo effect of PCPP on tumor hypoxia

Inspired by the good performance of PCPP in vitro, the in vivo effect of PCPP was then studied on CT26-tumor-bearing mice model. First, Cy5.5-modified PCPP was constructed and the biodistribution of the nanoparticles was investigated. Fig. S6 shows that PCPP can selectively accumulate in tumor region owing to the EPR effect, which suggested the great potential of PCPP for tumor targeted PFD delivery. Then, CT26-tumor-bearing mice were continuously injected with PCPP, CPP, or PBS via tail vein for 7 days and sacrificed on the 10th day. The tumor tissues of mice were collected and the levels of collagen I and HA, two of the major components of ECM in tumor tissues were assessed by immunofluorescence staining. As shown in Fig. 3A and Fig. S7, compared with CPP treatment that had no obvious effect on the collagen I and HA levels, the green fluorescence corresponding to collagen I and HA dramatically decreased about 78% and 71% by PCPP treatment, indicating the effective ECM depletion effect of PCPP. Besides, the decreased expression of Collagen I in tumor after PCPP treatment was also confirmed by Western blot analysis (Fig. S8). Meanwhile, It was found that PCPP induced obvious down-regulation of transforming growth factor-β1 (TGF-β1) expression in tumor tissues as evidenced by Western blot analysis (Fig. S9), which was consistent with the previous report that PFD inudces ECM depletion mainly by suppressing the TGF-β1 signaling pathway [41]. Moreover, the reduction of tumor ECM was supposed to decrease the solid stress of tumors and make them less stiff, which resulting in lower elastic modulus and weaker resistence to compression (Fig. 3B). Therefore, the elastic modulis of tumors from mice that sacrificed on the 10th day were also measured. As shown in Fig. 3C. PCPP treatment reduced the elastic modulus of tumors by over 30%, demonstrating the solid stress of tumor was remarkabley alleviated. Importantly, benefiting from the decreased solid stress of tumor, the effective tumor vasculature area of PCPP group was dramatically inceased (Fig. 3D and E). This was mainly attributed to the decreased squeeze to blood vessels by ECM and favorable for the oxygen and nanoparticle delivery to tumor regions. Notably, the total area of tumor vessels showed no significant change after PCPP or CPP treatment (Fig. S10), indicating that either CPP or PCPP treatment would not affect tumor angiogenesis. Furthermore, the reduced tumor ECM as well as the increased effective tumor vascularture density were expected to improve the oxygen supply in tumor, thus alleviating tumor hypoxia. To verify this, an NIR fluorescent probe Cy7-NO_2 which shows a distinct response to overexpressed nitroreductase (NTR) in hypoxic cells was synthesized and utilized for tumor hypoxia detection in vivo (Fig. S11 and Fig. 3F) [42]. In particular, after treated with PBS, CPP, or PCPP for 7 days, mice were intravenously injected with Cy7-NO_2 on the 10th day and the fluoresncence images of mice were then collected. It can been seen that the tumors of all groups showed a significant enhancement in fluorescence intensity within 2 h and reached a maxima at 8 h post injection (Fig. S12), indicating the hypoxic state of the solid tumors. Notably, the fluorescence intensity of tumor in PCPP group was much lower than that in CPP or PBS group (Fig. 3G), demonstrating the less hypoxic of tumors from PCPP group. Moreover, the tumors of mice from different groups were also collected at 12 h post Cy7-NO_2 injection. And the fluorescence intensity of the excised tumors from PCPP group was obvously lower than that from CPP or PBS group (Fig. 3G), further revealing the hypoxia state of tumors was effectively alleviated by PCPP treatment. Apart from these, the relieved hypoxia of tumors after PCPP treatment was also verified by the much weaker fluorescence of hypoxia inducible factor-alpha (HIF-α) and pimonidazole (PIMO) in tumor slices by immunohistochemistry staining (Fig. 3H and Fig. S13) [43]. Further Western blot analysis also revealed the decreased expression of HIF-α in tumor after PCPP treatment (Fig. S8). Both of these provided additional evidence for the improved oxygen supply in tumor regions by PCPP treatment.

3.4. In vivo effect of PCPP on tumor uptake of NM-PPIX

Furthermore, whether the depletion of tumor ECM by PCPP treatment would enhance the tumor uptake of NM-PPIX was studied. As shown in Fig. 4A, mice continuously treated with PBS, CPP, or PCPP for 7 days were intravenously injected with NM-PPIX on the 10th day, then the in vivo biodistribution of NM-PPIX in mice were monitored by a small animal fluorescent imaging system. As shown in Fig. 4B,D, mice from PCPP group had a quick and specific accumulation of NM-PPIX in tumor tissues, showing much stronger fluorescence signal in comparison with those from CPP or PBS group. Besides, ex vivo fluorescence imaging of tumors and major organs from the mice sacrificed at 24 h post NM-PPIX injection also indicated the higher accumulation of NM-PPIX in PCPP treated group than that in the others (Fig. 4C,E). These results demonstrated that PCPP mediated tumor ECM depletion can significantly improve the tumor uptake of NM-PPIX in vivo. It should be pointed out that although PCPP greatly enhanced the accumulation of NM-PPIX in tumor, the biodistribution of NM-PPIX in major organs (hearts, livers, spleens, lungs, and kidneys) was almost unaffected (Fig. 4C,E), which was mainly due to the high tumor selectivity of PCPP.

3.5. In vivo anti-tumor effect and biosafety evaluation

Motivated by the alleviated tumor hypoxia and enhanced tumor uptake of NM-PPIX by PCPP pre-treatment, then whether the in vivo PDT effect can be enhanced with the assist of PCPP was assessed. 25 of CT26-tumor-bearing mice were randomly divided into 5 groups and treated differently according to the timeline in Fig. 5A (Group 1: PBS; Group 2: PCPP + NM-PPIX; Group 3: NM-PPIX + laser; Group 4: CPP + NM-PPIX + laser; Group 5: PCPP + NM-PPIX + laser). The tumor volume and body weight of mice were recorded every 3 days. As displayed in Fig. 5B, PCPP + NM-PPIX (Group 2) exhibited negligible effect on tumor inhibition, indicating the low toxicity of both PCPP and NM-PPIX which were consistent with the in vitro cytotoxicity results (Fig. S14). Besides, compared with NM-PPIX + laser (Group 3) or CPP + NM-PPIX + laser (Group 4), PCPP + NM-PPIX + laser (Group 5) showed much better tumor inhibition effect during the experiment. The tumor inhibition rate of Group 5 was 92% on the 19th day, which was remarkably higher than that of Group 3 (65%) and Group 4 (62%). This clearly demonstrated that PCPP treatment can effectively enhance tumor PDT in vivo. Interestingly, further study also showed that PCPP treatment had much stronger enhancement effect on PDT when compared with PFD treatment, which was mainly attribute to the EPR effect of the nanoparticles (Fig. S15). Moreover, since tumor PDT effect depends strongly on the local ROS generation, we also detected the in vivo ROS generation in tumor tissues of different groups by using a luminescent probe, L-012, which could show obvious luminescent signal in the presence of ROS [44]. As shown in Fig. 5C, mice from different groups were intratumorally injected with L-012 at 12 h just before laser irradiation was given. Then mice were observed by using a small animal imaging system. Fig. 5D shows that mice treated with ether PBS (Group 1) or PCPP + NM-PPIX (Group 2) showed no detectable lumincescent signal in tumors, demonstrating such treatments would not lead to ROS generation in tumor regions. However, for mice treated with NM-PPIX + laser (Group 3) or CPP + NM-PPIX + laser (Group 4), or PCPP + NM-PPIX + laser (Group 5), obvious lumincescent signals in tumor regions were observed which indicated the successful ROS generation in vivo. Notably, the singal strength of Group 5 was much

stronger than that of Group 3 and Group 4, demonstrating the much more ROS generation in tumor regions of Group 5, which was consistent with the better tumor PDT effect of Group 5. Additionally, the body weight of mice from all groups showed no significant difference during the 19 days experiment (Fig. 5E), demonstrating the low systemic toxicity of PCPP treatment. Importantly, mice from various groups were sacrificed on the 19th day. Both the size and tumor weight results (Fig. 5F) indicated the enhancement of tumor PDT by PCPP treatment, clearly revealed the effectiveness of ECM depletion by PCPP on PDT enhancement. Furthermore, compared with Group 3 and Group 4, tumor tissues of mice from Group 5 showed more caspase-3 and less B-cell lymphoma-2 (bcl-2) expressions, which also indicated the enhancement of PDT effect by PCPP (Fig. 5G and H). Finally, the tumor tissues of mice were also collected for hematoxylin-eosin (H&E) and TdT-mediated dUTP nick-end labeling (TUNEL) staining after the treatments and the results also showed the enhanced tumor suppression performance of Group 5 in which more cellular apoptosis and death were observed than that of Group 3 or Group 4 (Fig. 5I). It was worth mentioning that the blood biochemical test results showed that no significant difference was found in the levels of aspartate transaminase (AST) and glutamic pyruvate transaminase (ALT) in serum of mice after PCPP treatment (day 19) (Fig. 5J). Meanwhile, the H&E staining of tumor tissues (Fig. S16) on the 19th day also showed that no detectable toxicity was induced by PCPP treatment. Both of these revealed the good biosafety of PCPP.

3.6. Metastasis evaluation

Although PCPP treatment can effectively enhance tumor PDT of NM-PPIX by remodeling tumor ECM, one possible drawback is that the decrease of the dense tumor matrix and the opening of tumor blood vessel may increase the formation of metastases [45,46]. To examine the effect of PCPP treatment on tumor metastasis, mice after various treatments were sacrificed on the 35th day and the lung sections of them were collected for H&E staining. As shown in Fig. 6, compared with Group 1 that considerable number of metastatic regions were observed in the lung section, mice with PCPP treatment (Group 2 and Group 5) showed no obvious metastatic sites in the lungs. The significantly decreased metastasis level in lungs indicated the anti-metastasis effect by modulating the tumor ECM after PCPP treatment due to the PCPP mediated alleviation of the hypoxic tumor microenvironment, which is a driving force for tumor cells to metastasize [47,48].

4. Conclusion

In summary, a functional COF-based tumor ECM remodeling nanosystem PCPP was fabricated to enhance tumor PDT. PCPP could selectively accumulate in tumor regions and release anti-fibrotic drug PFD in situ to down-regulate the ECM compenents such as HA and collagen I. Such depletion of tumor ECM largely decreased the solid stress of tumor, realizing greatly alleviated hypoxic state of tumor. Furthermore, tumor ECM depletion caused by PCPP treatment also significantly improved the tumor homing of subsequently injected NM-PPIX. Both the relieved hypoxia state and improved uptake of NM-PPIX in tumor resulted in greatly promoted ROS generation to acheive remarkably enhanced tumor PDT effect in vivo. Additionally, PCPP was proved to induce negligible systemic toxicity and also decreased the metastasis level of tumor.

Notes

The authors declare no competing financial interest.

Data availability

The raw/processed data required to reproduce these findings are available from the authors.

Acknowledgements

This work was supported by the National Natural Science Foundation of China (51833007, 51873162 and 51690152). Authors Shi-Bo Wang and Zhao-Xia Chen contributed equally to this work.

Appendix A. Supplementary data

Supplementary data to this article can be found online at https://doi.org/10.1016/j.biomaterials.2020.119772.

References

[1] Y. Lu, A.A. Aimetti, R. Langer, Z. Gu, Bioresponsive materials, Nat. Rev. Mater. 2 (2017) 16075.
[2] C. He, D. Liu, W. Lin, Self-assembled core-shell nanoparticles for combined chemotherapy and photodynamic therapy of resistant head and neck cancers, ACS Nano 9 (2015) 991–1003.
[3] A.P. Castano, P. Mroz, M.R. Hamblin, Photodynamic therapy and anti-tumour immunity, Nat. Rev. Cancer 6 (2016) 535.
[4] S. Ye, J. Rao, S. Qiu, J. Zhao, H. He, Z. Yan, T. Yan, Y. Deng, H. Ke, H. Yang, Y. Zhao, Z. Guo, H. Chen, Rational design of conjugated photosensitizers with controllable photoconversion for dually cooperative phototherapy, Adv. Mater. 30 (2018) 1801216.
[5] M. Triesscheijn, P. Baas, J.H. Schellens, F.A. Stewart, Photodynamic therapy in oncology, The Oncologist 11 (2016) 1034–1044.
[6] H. Maeda, J. Wu, T. Sawa, Y. Matsumura, K. Hori, Tumor vascular permeability and the EPR effect in macromolecular therapeutics: a review, J. Control. Release 65 (2000) 271–284.
[7] S. Zhen, X. Yi, Z. Zhao, X. Lou, F. Xia, B.Z. Tang, Drug delivery micelles with efficient near-infrared photosensitizer for combined image-guided photodynamic therapy and chemotherapy of drug-resistant cancer, Biomaterials 218 (2019) 119330.
[8] L.H. Liu, W.X. Qiu, Y.H. Zhang, B. Li, C. Zhang, F. Gao, L. Zhang, X.Z. Zhang, Adv. Funct. Mater. 27 (2017) 1700220.
[9] A.L. Harris, Hypoxia-a key regulatory factor in tumor growth, Nat. Rev. Cancer 2 (2012) 38.
[10] C. Qian, P. Feng, J. Yu, Y. Chen, Q. Hu, W. Sun, X. Xiao, X. Hu, A. Bellotti, Q. Shen, Z. Gu, Anaerobe-inspired anticancer nanovesicles, Angew. Chem. Int. Ed. 56 (2017) 2588–2593.
[11] R.K. Jain, Normolizing tumor vasculature with anti-angiogenic therapy: a new paradigm for combination therapy, Nat. Med. 7 (2001) 987.
[12] K.C. Valenburg, A.E. de Groot, K.J. Pienta, Targeting the tumour stroma to improve cancer therapy, Nat. Rev. Clin. Oncol. 15 (2018) 366.
[13] C. Feig, A. Gopinathan, A. Neesse, D.S. Chan, N. Cook, D.A. Tuveson, The pancreas cancer microenvironment, Clin. Cancer Res. 18 (2012) 4266–4276.
[14] W. Fang, M. Yao, N. Cheng, Priming cancer cells for drug resistance: role of the fibroblast niche, Front. Biol. 9 (2014) 114.
[15] D.F. Camacho, K.J. Pienta, Disrupting the networks of cancer, Clin. Cancer Res. 18 (2012) 2801–2808.
[16] C.C. Maley, Classifying the evolutionary and ecological features of neoplasms, Nat. Rev. Cancer 17 (2017) 605.
[17] D. Hanahan, R.A. Weinberg, Hallmarks of cancer: the next generation, Cell 144 (2011) 646–674.
[18] K. Shiga, Cancer-associated fibroblasts: their characteristics and their roles in tumor growth, Cancers 7 (2015) 2443-2438.
[19] R.O. Hynes, A. Naba, Overview of the matrisome-an inventory of the extracellular matrix constituents and functions, Cold Spring Harb. Perspect. Biol. 4 (2012) a004903.
[20] C. Bonnans, J. Chou, Z. Werb, Remodelling the extracellular matrix in developments and disease, Nat. Rev. Mol. Cell Biol. 15 (2014) 786–801.
[21] R.O. Hynes, The extracellular matrix: not just pretty fibrils, Science 326 (2009) 1216–1219.
[22] G.J. Laurent, R.C. Chambers, M.R. Hill, R.J. McAnulty, Regulation of matrix turnover: fiblasts, forces, factors and fobrosis, Biochem. Soc. Traans. 35 (2007) 647–651.
[23] R. Kalluri, M. Zeisberg, Fiblasts in cancer, Nat. Rev. Cancer 6 (2006) 392–401.
[24] X. Feng, X. Ding, D. Jiang, Covalent organic framworks, Chem. Soc. Rev. 41 (2012) 6010–6022.
[25] P.J. Waller, F. Gandara, O.M. Yaghi, Chemistry of covalent organic frameworks, Acc. Chem. Res. 48 (2015) 3053–3063.
[26] S. Lin, C.S. Diercks, Y.B. Zhang, N. Kornienko, Covalent organic frameworks comprising cobalt porphyrins for catalytic CO2 reduction in water, Science 349 (2015) 1208–1213.
[27] L. Chen, Photoelectric covalent organic frameworks: converting open lattices into ordered donor–acceptor heterojunctions, J. Am. Chem. Soc. 136 (2014) 9806–9809.
[28] H. Xu, D. Jiang, Covalent organic frameworks: crossing the channel, Nat. Chem. 6 (2014) 564–566.
[29] Q. Sun, B. Aguila, J. Perman, N. Ngugen, S. Ma, Flexibility matters: cooperative

active sites in covalent organic framework and threaded ionic polymer, J. Am. Chem. Soc. 138 (2016) 15790–15796.
[30] P. Pachfule, A. Acharjya, J. Roeser, T. Langenhahn, M. Schwarze, R. Schomäcker, A. Thomas, J. Schmidt, Diacetylene functionalized covalent organic framework (COF) for photocatalytic hydrogen generation, J. Am. Chem. Soc. 140 (2018) 1423–1427.
[31] L. Bai, Nanoscale covalent organic frameworks as smart carriers for drug delivery, Chem. Commun. 52 (2016) 4128–4131.
[32] M.L. Xu, L.Y. Wang, Y. Xie, Y.H. Song, L. Wang, Ratiometric electrochemical sensing and biosensing based on multiple redox-active state $COF_{DHTA\text{-}TTA}$, Sens. Actuators B Chem. 281 (2019) 1009–1015.
[33] S. Mitra, H.S. Sasmal, T. Kundu, S. Kandambeth, K. Illath, D.D. Diaz, R. Banerjee, Targeted drug delivery in covalent organic nanosheets (CONs) via sequential postsynthetic modification, J. Am. Chem. Soc. 139 (2017) 4513–4520.
[34] Q. Fang, J. Wang, S. Gu, R.B. Kaspar, Z. Zhuang, J. Zheng, H. Guo, S. Qiu, Y. Yan, 3D porous crystalline polyimide covalent organic frameworks for drug delivery, J. Am. Chem. Soc. 137 (2015) 8352–8355.
[35] G. Zhang, X. Li, Q. Liao, Y. Liu, K. Xi, W. Huang, X. Jia, Water-dispersible PEG-curcumin/amine functionalized covalent organic framework nanocomposites as smart carriers for in vivo drug delivery, Nat. Commun. 9 (2018) 2785.
[36] L. Richeldi, U. Yasothan, P. Kirkpatrick, Pifenidone, Nat. Rev. Drug Discov. 10 (2011) 489–490.
[37] Q. Hao, C. Zhao, B. Sun, C. Lu, J. Liu, M. Liu, L. Wan, D. Wang, Confined synthesis of two-dimensional covalent organic framework thin films within superspreading water layer, J. Am. Chem. Soc. 140 (2018) 12152–12158.
[38] J. Cheng, B.A. Teply, I. Sherifi, J. Sung, G. Luther, F.X. Gu, E. Levy-Nissnbaum, A.F. Radovic-Moreno, R. Langer, O.C. Farokhzad, Formulation of functionalized PLGA–PEG nanoparticles for in vivo targeted drug delivery, Biomaterials 28 (2007) 869–876.
[39] Q. Lei, S.B. Wang, J.J. Hu, Y.X. Lin, C.H. Zhu, L. Rong, X.Z. Zhang, Stimuli-responsive “cluster bomb” for programmed tumor therapy, ACS Nano 11 (2017) 7201–7214.
[40] Z.X. Chen, M.D. Liu, M.K. Zhang, S.B. Wang, L. Xu, C.X. Li, F. Gao, B.R. Xie, Z.L. Zhong, X.Z. Zhang, Interfering with lactate-fueled respiration for enhanced photodynamic tumor therapy by a porphyrinic mof nanoplatform, Adv. Funct. Mater. 28 (2018) 1803498.
[41] F.S. Shihab, W.M. Bennett, H. Yi, T.F. Andoh, Pirfenidone treatment decreases transforming growth factor-β1 and matrix proteins and ameliorates fibrosis in chronic cyclosporine nephrotoxicity, Am. J. Transplant. 2 (2002) 111–119.
[42] J.R. Zheng, Y.Z. Shen, Z.Q. Xu, Z.W. Yuan, Y.Y. He, W. Chen, E. Murat, J. Yin, H.Y. Chen, Near-infrared off-on fluorescence probe activated by NTR for in vivo hypoxia imaging, Biosens. Bioelectron. 119 (2018) 141–148.
[43] M.K. Zhang, C.X. Li, S.B. Wang, T. Liu, X.L. Song, X.Q. Yang, J. Feng, X.Z. Zhang, Tumor starvation induced spatiotemporal control over chemotherapy for synergistic therapy, Small 14 (2018) 1803602.
[44] W. Wan, Y. Lin, H. Chen, C. Huang, P. Shih, Y. Bow, W. Chia, H. Sung, In situ nanoreactor for photosynthesizing H_2 gas to mitigate oxidative stress in tissue inflammation, J. Am. Chem. Soc. 139 (2017) 12923–12926.
[45] C. Stockmann, A. Doedens, A. Weidemann, N. Zhang, N. Takeda, J.I. Greenberg, D.A. Cheresh, R.S. Johnson, Deletion of vascular endothelial growth factor in myeloid cells accelerates tumorigenesis, Nature 456 (2008) 814.
[46] A.D. Rhim, E.T. Mirek, N.M. Aiello, A. Maitra, J.M. Bailey, F. McAllister, M. Reichert, G.L. Beatty, A.K. Rustgi, R.H. Vonderheide, S.D. Leach, B.Z. Stanger, EMT and dissemination precede pancreatic tumor formation, Cell 148 (2012) 349–361.
[47] E.B. Rankin, A.J. Giaccia, Hypoxic control of metastasis, Science 352 (2016) 175–180.
[48] D.M. Gilkes, G.L. Semenza, D. Wirtz, Hypoxia and the extracellular matrix: drivers of tumour metastasis, Nat. Rev. Cancer 14 (2014) 430.